Article:
Pan, P., Moorehead, R.D. and Hayward, T.J. (2020) Influence of geometry on the giant magnetoimpedance of high-aspect ratio amorphous magnetic ribbons. Journal of Applied Physics, 128 (17). 174504. ISSN: 0021-8979

https://doi.org/10.1063/5.0022777

Influence of Geometry on the Giant Magnetoimpedance of High-Aspect Ratio Amorphous Magnetic Ribbons

Patrick Pan[1], Robert. D. Moorehead[2] and T. J. Hayward[1]

[1]Department of Materials Science and Engineering, University of Sheffield, United Kingdom (U.K.)

[2]The Henry Royce Institute and Department of Materials Science and Engineering, The University of Sheffield, Sir Robert Hadfield Building, Sheffield, S1 3JD, United Kingdom (U.K.)

Abstract

We study the influence of ribbon geometry on the giant magnetoimpedance behaviour of both low- and high-aspect ratio (*length (l) /width (w)* = 2 to 150) ribbons made from commercially available amorphous magnetic materials. Our results indicate that the variation of the ribbons' GMI with geometry is due to the combination of edge effects (due to damage created by the ribbon cutting process) and global shape anisotropy. In high-aspect ratio ribbons (*length (l) /width (w)* $\geq$ 20) we find that the GMI decreases with width, which we suggest is due to the cutting process creating induced stresses that suppresses the transverse susceptibility at the edge of the material. In lower aspect ratio ribbons (*length (l) /width (w)* $\leq$ 20), shape anisotropy results in a relatively rapid increase in GMI with increasing length. We conclude that, with suitable optimisation, high-aspect ratio ribbons prepared from commercially available materials are suitable for use as macro-scale sensors that detect small magnetic fields/strains over a large sensing area.

1. Introduction

There has been long-term interest in designing giant magnetoimpedance (GMI) sensors based on amorphous magnetic ribbons [1]–[5]. GMI sensors utilises the GMI effect which is defined as a large change of electrical impedance of a magnetic material when subjected to an applied dc magnetic field. The magnitude of the GMI effect typically peaks at a 'critical frequency' of AC current (f_0) between 2 – 7MHz, with the precise value depending ribbon material and the conditions under which it has been processed [2]. At these frequencies the GMI effect is dominated by the skin effect: applied magnetic fields alter a ribbon's transverse permeability, producing large changes in the skin-depth of the AC current passing through it. Thus, large variations in electrical impedance are observed as the applied magnetic field is varied [2], [6]. GMI ratios as large as several hundred percent [2] can be

observed when both the microstructure and domain structure of ribbons are well-optimised [7], [8].

It has been reported that the GMI effect is strongly dependent on ribbon geometry [9]–[14]. For example, Ding *et. al.* [10] observed that amorphous ribbons show a sharp decrease in GMI ratio for ribbons with aspect ratios (length (l)/width (w)) below 5.4, and a similar trend was observed by Chaturvedi et. al. [9] where a decrease in GMI was seen for ribbons with lengths below 8mm. In both cases these trends were attributed to demagnetising effects/shape anisotropy. However, there have been relatively few studies of the geometry dependence of the GMI effect in high-aspect ratio ($l/w \geq 20$) amorphous ribbons. There are instances where high-aspect ratio ribbons could be useful as GMI sensors, with the large signals available meaning that macroscopic sensors could allow detection of relatively small stimuli distributed over large areas or local stimuli that affect only small areas of a larger sensor. For example, one can envisage such sensors being mass deployed to monitor the structural integrity of containers containing hazardous waste, where either global swellings or local deformations could be symptoms of container failure.

The magnitude of a ribbon's GMI response is also strongly influenced by its saturation magnetostriction coefficient λ_s [15], [16]. This controls the strength and orientation of stress-induced anisotropies, which in turn dictate domain structure and permeability. However, substantial changes in GMI ratios can also be induced by performing additional processing [16], [17]. For example, many studies that report that the GMI ratios of amorphous ribbons can be improved by post-fabrication thermal annealing due to the relaxation of induced strains [10], [18]–[20]. Hence, the material becomes magnetically softer making it more effective as a GMI sensor. However, it is also interesting to examine whether as manufactured, commercially available amorphous materials can show strong enough GMI performance to be technologically useful, as this would likely offer a cost-effective route to deployment where either modest quantity of sensors are required, or bespoke sensor geometries must be fabricated from generic feedstocks.

In this paper we investigated how the GMI performance of three different, commercially available amorphous magnetic materials varies when they are fabricated into ribbon geometries with both high ($l/w \geq 20$) and low ($l/w \leq 20$) aspect ratios. Our results showed that there was substantial variation of the GMI ratio with geometry in both low- and high-

aspect ratio ribbons due to the combination of global shape anisotropy and edge effects resulting from the ribbon cutting process.

2. Experimental Methods

2.1 Basic Characterisation

Commercially available amorphous magnetic materials with chemical compositions $Co_{66}Si_{15}B_{14}Fe_4Ni_1$ (Co-rich), $Fe_{81}B_{13}Si_{3.5}C_2$ (Fe-rich) and $Ni_{40}Fe_{40}Si+B_{19}Mo_{1\text{-}2}$ (Ni-rich) were obtained as 25 µm thick foils from Goodfellow. We chose to study these three materials due to the relatively large differences in their magnetostriction constants (λ_s, Table 1, as quoted by the supplier).

Ribbon sample	Magnetostriction Coefficient λ_s (ppm)	Remanence ratio (M_r/M_s)	Saturation Flux Density (T)
$Co_{66}Si_{15}B_{14}Fe_4Ni_1$ (Co-rich)	< 1	0.82	0.55
$Fe_{81}B_{13}Si_{3.5}C_2$ (Fe-rich)	30	0.70	1.6
$Ni_{40}Fe_{40}Si+B_{19}Mo_{1\text{-}2}$ (Ni-rich)	8	< 1	0.8

Table 1. Magnetostriction coefficients, remanence ratio and saturation flux density values for $Co_{66}Si_{15}B_{14}Fe_4Ni_1$, $Fe_{81}B_{13}Si_{3.5}C_2$ and $Ni_{40}Fe_{40}Si+B_{19}Mo_{1\text{-}2}$ ribbons, as quoted by the supplier [24]–[26]**.**

To confirm the material properties quoted by the supplier we performed several basic characterisations of the foils: X-ray diffraction (XRD) with Cu K α radiation was conducted to analyse the crystal structure (2θ) of each material. Room temperature hysteresis loop measurements were performed using a superconducting quantum interference device (SQUID). For these measurements, each ribbon sample had common dimensions of 10mm x 2mm x 25 microns and were measured with magnetic fields (-150 Oe to 150 Oe) parallel to the ribbon samples' long axis. Finally, the surface roughness of each material was analysed using atomic force microscopy (Bruker Fastscan AFM) in tapping mode.

2.2. Sample Preparation

We prepared ribbons of the three materials by mechanically cutting them from the pre-cursor foils. Four batches of samples were cut, as shown in Table 2: Samples in Batch 1 had common lengths and widths of 400mm and 3mm, respectively; samples in Batch 2 had a fixed width of 10 mm, and lengths between 20 mm and 150 mm. Thus, Batch 2 covers aspect ratios in the range 2 to 15, similar to those that have been widely studied [21]–[23],

[27]. Samples in Batch 3 had fixed lengths of 300mm and widths in the range 2 mm to 10 mm. Thus, Batch 2 covered aspect ratio in the range 20 to 150, higher than those that have been typically studied. The ribbons in Batch 2 and 3 had both edges mechanically cut from the precursor foils; we classify these samples as Double Longitudinal Edge Cut (DLEC) ribbons. To investigate how the cutting process affected the GMI response of the ribbons we also manufactured Batch 4, which consisted of ribbons with dimensions equivalent to those in Batch 3, but where only a single edge was mechanically cut from the precursor foil (the other edge being that of the original foil). We classify these samples as Single Longitudinal Edge Cut (SLEC) ribbons. We chose to investigate the effects of the cutting process in samples with fixed width and varying lengths because we expected it to manifest as an edge effect, and thus have a more pronounced effect on samples with varying width than in those with varying length.

<table>
<tr><th rowspan="3">Chemical Composition</th><th colspan="6">Double Longitudinal Edge Cut (DLEC)</th></tr>
<tr><th colspan="2">Batch 1</th><th colspan="2">Batch 2</th><th colspan="2">Batch 3</th></tr>
<tr><th>Length</th><th>Width</th><th>Length</th><th>Width</th><th>Length</th><th>Width</th></tr>
<tr><td>$Co_{66}Si_{15}B_{14}Fe_4Ni_1$ (Co-rich)</td><td rowspan="3">400mm</td><td rowspan="3">3mm</td><td rowspan="3">20, 40, 60, 80, 100, 120, 140 and 150mm</td><td rowspan="3">10mm*</td><td rowspan="3">300mm*</td><td>4, 5, 6, 7, 8, 9 and 10mm</td></tr>
<tr><td>$Fe_{81}B_{13}Si_{3.5}C_2$ (Fe-rich)</td><td rowspan="2">2, 3, 4, 5, 6, 7, 8, 9 and 10mm</td></tr>
<tr><td>$Ni_{40}Fe_{40}Si+B_{19}Mo_{1-2}$ (Ni-rich)</td></tr>
<tr><td rowspan="3"></td><th colspan="6">Single Longitudinal Edge Cut (SLEC)</th></tr>
<tr><th colspan="6">Batch 4</th></tr>
<tr><th colspan="4">Length</th><th colspan="2">Width</th></tr>
<tr><td>$Co_{66}Si_{15}B_{14}Fe_4Ni_1$</td><td colspan="4" rowspan="3">300mm*</td><td colspan="2">4, 5, 6, 7, 8, 9 and 10mm</td></tr>
<tr><td>$Fe_{81}B_{13}Si_{3.5}C_2$</td><td colspan="2" rowspan="2">3, 4, 5, 6, 7, 8, 9 and 10mm</td></tr>
<tr><td>$Ni_{40}Fe_{40}Si+B_{19}Mo_{1-2}$</td></tr>
</table>

Table 2. List of ribbon samples made from each of the three materials studied, with either DLEC or SLEC edge profiles. Dimensions labelled with (*) are fixed within a given batch of samples. To summarise: (DLEC) Batch 1 are ribbon samples with common dimensions of 400mm x 3mm; Batch 2 ribbon samples have a varying length with a fixed width of 10mm; Batch 3 ribbon samples have a fixed length of 300mm and varying widths; (SLEC) Batch 4 ribbon samples have a fixed length of 300mm and varying widths.

2.2 Magneto-impedance measurements

The measurement geometry used to characterise the ribbons' GMI behaviours is illustrated schematically in Fig. 1. The impedance of the ribbons was measured in the range 100 kHz to 10 MHz using a 4-terminal connection to an Agilent 4294A precision impedance analyser. To prevent distortion of the ribbon sample during measurement they were supported by a plastic mount sandwiching the ribbon, which was then placed at the centre of an electromagnet. The electromagnet supplied dc magnetic fields up to H = ±150 Oe to the ribbons.

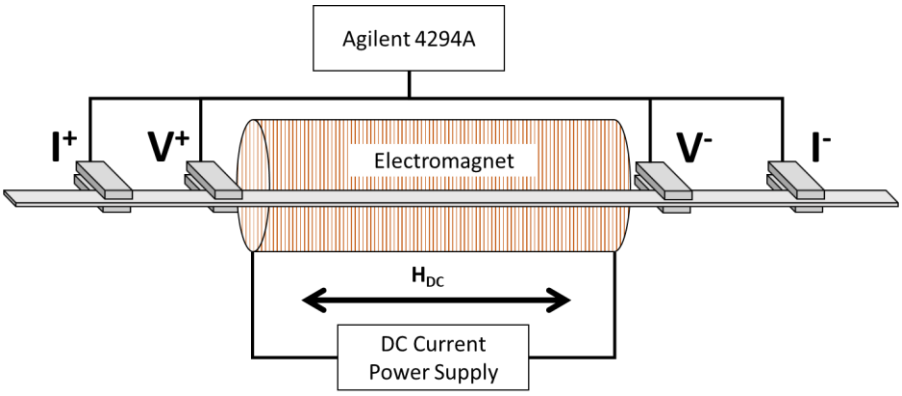

Fig. 1. Schematic diagram of experimental setup used to measure the magnetoimpedance of the amorphous ribbon samples.

Two electromagnets were used to apply magnetic fields to the ribbon samples: A Helmholtz coil with a uniform field region ~150 mm long was used to measure the Batch 1 samples, whereas a 200 mm long solenoid was used to measure Batch 2, 3 and 4. When measuring with the Helmholtz coil both current contacts (I^+, I^-) and voltage contacts (V^+, V^-) were connected to the ends of the ribbons. When measuring using the solenoid, current contacts were connected at the ends of the ribbon whereas the voltage contacts were connected to the ribbons at the ends of the solenoid, such that the impedance analyser characterised only the sections of the ribbons to which the field was applied.

The field-dependent impedance values measured from the setup were used to calculate the GMI values of the ribbons using the standard expression:

$$GMI = \frac{|Z(H)| - |Z(H_{max})|}{|Z(H_{max})|} \times 100\% \qquad \text{(equation 1)}$$

where $|Z(H_{max})|$) is the absolute impedance measured at the maximum DC magnetic field applied. Parasitic impedances were minimised by using short, 0.14m long, BNC to crocodile clip test leads [28] and by performing an open, short and load calibrations on the impedance analyser.

Despite the steps taken to calibrate the impedance measurements, parasitic impedances were still present at the connection between the crocodile clips and the ribbon samples. To characterise these contributions, we placed the voltage contacts next to each other without touching (making the distance of the ribbon between the contacts negligible) and measured the impedance spectrum. The highest value of $|Z|$ measured in this way from each batch was selected and used as a representative value of the parasitic impedance Z_p. Assuming that the (as measured) values of $|Z(H)|$ and $|Z(H_{max})|$ in equation 1 contained parasitic impedances the measured impedance could be expressed as $|Z(H)| = |Z_S(H) + Z_P|$ and $|Z(H_{max})| = |Z_S(H_{max}) + Z_P|$, where Z_S was the true impedance of the sample [29]. Thus, the measured GMI ratios were potentially suppressed by the Z_p, which was primarily expected to increase the denominator in equation 1. Therefore, we also calculated a corrected GMI ratio for each ribbon sample using:

$$GMI_{corrected} = \frac{|Z(H) - Z_P| - |Z(H_{max}) - Z_P|}{|Z(H_{max}) - Z_P|} \times 100\% \quad \text{(equation 2)}$$

In this paper we will present measurements both with and without these corrections applied, thus representing the upper and lower limits of the true ribbon samples' true GMI ratios.

2.3. Heat treating Fe-rich DLEC and SLEC samples

It is well-established that heat treating amorphous ribbons relaxes induced stresses, leading to larger GMI responses. To investigate whether heat treatments were capable of relaxing stresses induced by our mechanical cutting process, SLEC and DLEC Fe-rich ribbons with length = 180 mm, width = 4 mm and thickness = 25 µm were heat treated at 473K for 30 minutes in an argon environment. Fe-rich ribbons were selected for this study because of

their large λ_s values (Table 1), which were expected to make these materials more sensitive to induced stresses than equivalent Co-rich and Ni-rich ribbons.

3. Results and Discussion

3.1 Basic characterisations of Co-, Fe- and Ni-rich ribbons

The XRD measurements for all of the materials exhibited a single broad peak around 2θ = 45° angle (Fig. 2). This is a typical trait for an amorphous crystal structure and indicated that the materials had the expected microstructure [2], [21]–[23].

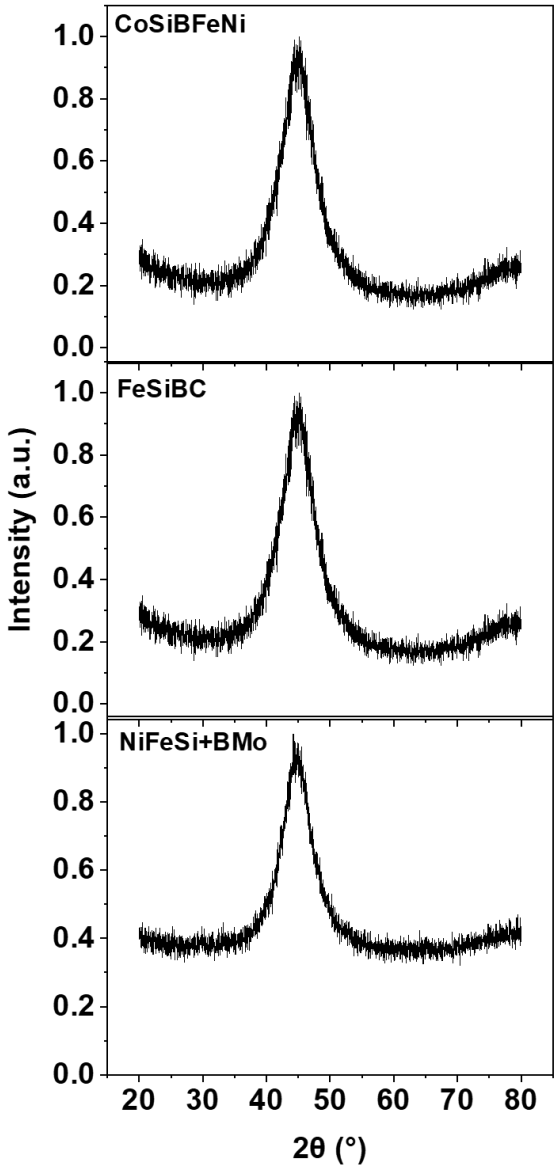

Fig. 2. XRD patterns measured from foils of $Co_{66}Si_{15}B_{14}Fe_4Ni_1$, $Fe_{81}B_{13}Si_{3.5}C_2$ and $Ni_{40}Fe_{40}Si+B_{19}Mo_{1\text{-}2}$ at ambient conditions.

Fig. 3(a) presents hysteresis loops for each of the materials. The loops show very small hysteresis and almost linear susceptibilities at low fields. The coercive fields measured for the samples were 0.01 Oe for $Co_{66}Si_{15}B_{14}Fe_4Ni_1$, 0.16 Oe for $Fe_{81}B_{13}Si_{3.5}C_2$ and 0.23 Oe for $Ni_{40}Fe_{40}Si+B_{19}Mo_{1\text{-}2}$ (Fig. 3 (b)). The data in Fig. 3 can be used to infer the susceptibility/permeability of the samples, with the Co-rich sample having the lowest susceptibility/permeability followed by Fe-rich sample and Ni-rich sample.

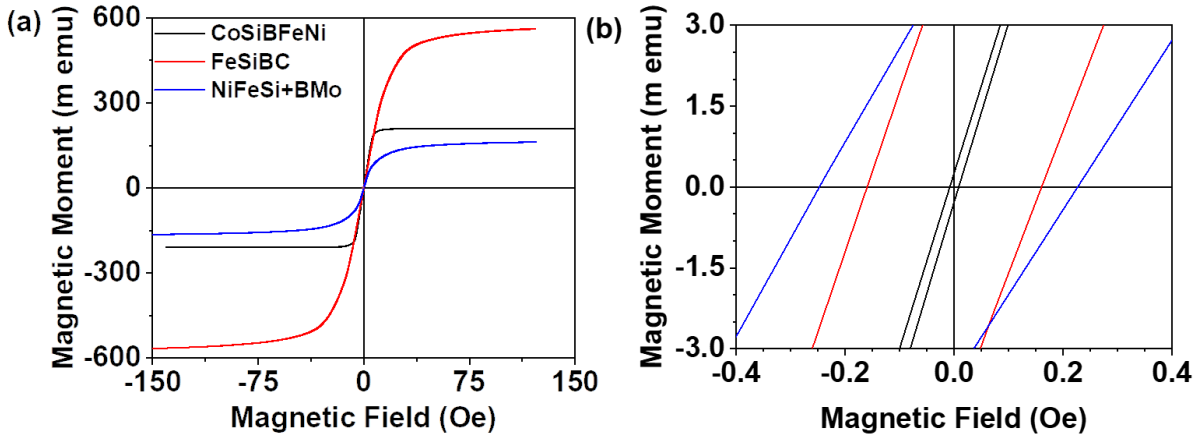

Fig. 3. (a) hysteresis loops of $Co_{66}Si_{15}B_{14}Fe_4Ni_1$, $Fe_{81}B_{13}Si_{3.5}C_2$ and $Ni_{40}Fe_{40}Si+B_{19}Mo_{1\text{-}2}$ samples with common dimensions of 10mm x 2mm x 25 microns. (b) A more detailed image of the centre of the loops, allowing their small coercive fields to be seen.

Fig. 4. presents AFM images of the each of the materials surfaces. We quantified the surface roughness using a root mean square (R_q) value, which was found to be 4.15nm for $Co_{66}Si_{15}B_{14}Fe_4Ni_1$, 15.3nm for $Fe_{81}B_{13}Si_{3.5}C_2$ and 14.8nm for $Ni_{40}Fe_{40}Si+B_{19}Mo_{1\text{-}2}$ samples (Fig. 3 (a-c)).

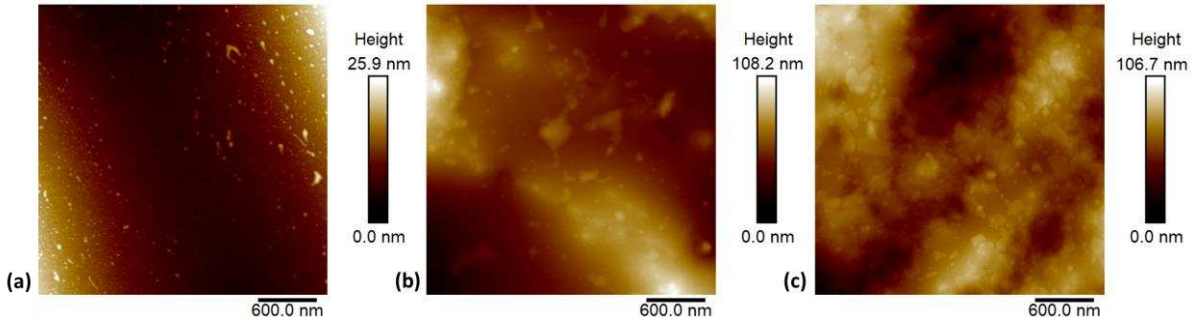

Fig. 4. AFM images of surface roughness of (a) $Co_{66}Si_{15}B_{14}Fe_4Ni_1$, (b) $Fe_{81}B_{13}Si_{3.5}C_2$ and (c) $Ni_{40}Fe_{40}Si+B_{19}Mo_{1\text{-}2}$ amorphous ribbon samples with common scanning area of 3x3 microns.

3.2 GMI behaviour of Co-, Fe- and Ni-rich ribbons

Fig. 5. (a) presents the field dependence of the GMI ratio for Batch 1 ribbon samples fabricated from each of the materials listed in Table 1. All three materials exhibit single-peaked GMI behaviour with GMI ratios of the order of tens of percent. Single peaked behaviour from amorphous ribbons is typically associated with low transverse anisotropies [30]. This would be expected for these ribbon samples where no special treatment was used to induce a transverse anisotropy following their cutting from the precursor foils. The Co-rich sample was found to have the highest GMI ratio (66.4%), with the Ni-rich (15.1%) and Fe-rich (10.2%) showing lower values. This was consistent with previous literature where larger GMI ratios typically occur in Co-rich amorphous metals compared to Fe- and Ni-rich materials [2], [28], [31], [32]. The GMI ratios also correlated well with the quasi-static magnetic susceptibilities/permeabilities implied by the ribbon's hysteresis loops. The Co ribbon showed the highest GMI and was substantially magnetically softer than Ni and Fe ribbons, which showed sequentially higher coercivities/lower susceptibilities and lower GMI ratios.

The magnitudes of the materials' GMI responses correlated inversely, with the size of the λ_s constants listed in Table 1, with Co-rich ribbon having the smallest value of λ_s, followed by the Ni-rich and Fe-rich ribbons. A positive correlation between the ribbons' λ_s constants and coercivities was observed. These findings were again consistent with previously published literature, where materials with negative and near-zero λ_s constants exhibited the largest GMI ratios [2] . Decreases in GMI ratios with increasing λ_s are typically attributed to increasing magnetoelastic anisotropies that supress the ribbons' permeabilities [16]. However, we note that previous studies have also shown GMI ratios to be influenced by surface roughness [34], [35]. In our samples, the Fe and Ni-rich ribbons had similar roughness', while the Co-rich ribbon had a much lower roughness. Therefore, it is possible that the differences in the ribbons' GMI responses resulted from a combination of differences in magnetostrictive properties and their surface topographies.

Fig. 5. (b) illustrates how the three ribbons' GMI ratios varied with frequency. The GMI ratios for all three ribbons peaked at a critical frequency (f_0) in the range 2 to 3 MHz. This was consistent with the ribbons' magnetoimpedance responses being primarily due to skin effect [2], [6]. At these frequencies the transverse permeability of the ribbons (which

controls the skin depth) likely resulted from a combination of domain wall motion and domain rotation [2], [6], [33]. At higher frequencies beyond f_0 domain wall motion becomes progressively damped by the eddy current losses and only magnetisation rotation contributes to the transverse permeability, thus decreasing GMI ratio.

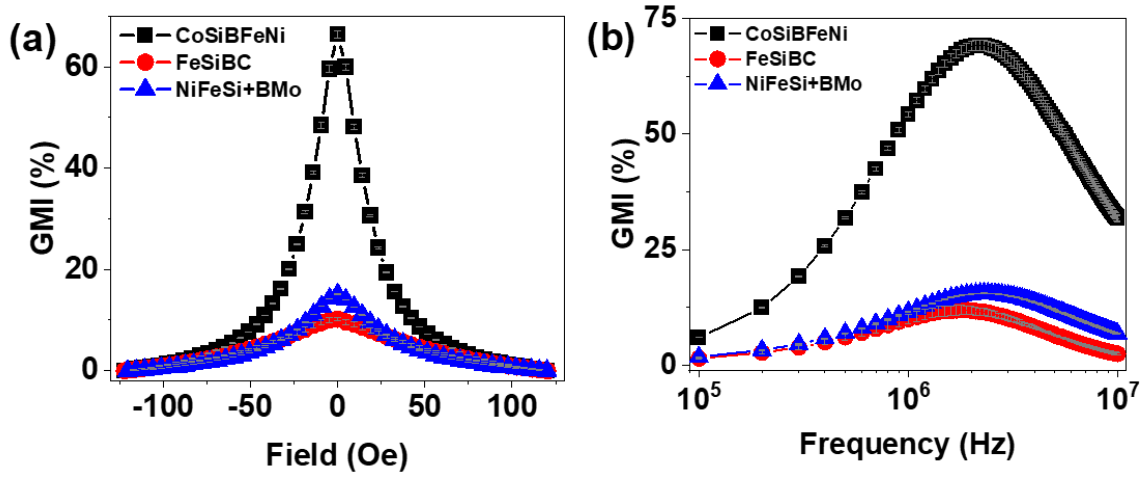

Fig. 5. (a) Variation of GMI with applied field at 3 MHz for three ribbons with different compositions and common dimensions of 400 mm x 3 mm x 25 µm and (b) frequency variation of the GMI ratio for the same ribbons.

3.2 Geometry dependence of GMI

a. Length dependence in low aspect ratio ribbons

Fig. 6. (a) presents the variation of the GMI ratio at f_0 with length for the Batch 2 ribbon samples. All three materials showed a common trend where the GMI ratio increased with ribbon length, and tended asymptotically towards a constant value for lengths > 120 mm. Fig. 6. (b) presents equivalent data for $GMI_{corrected}$. In these data the GMI ratios were enhanced over the uncorrected GMI values, but the basic trends remained. This indicated that the observed variations were genuinely due to effects of the ribbon geometry, rather than that of parasitic impedances, which were expected to be most significant when measuring the shortest ribbons.

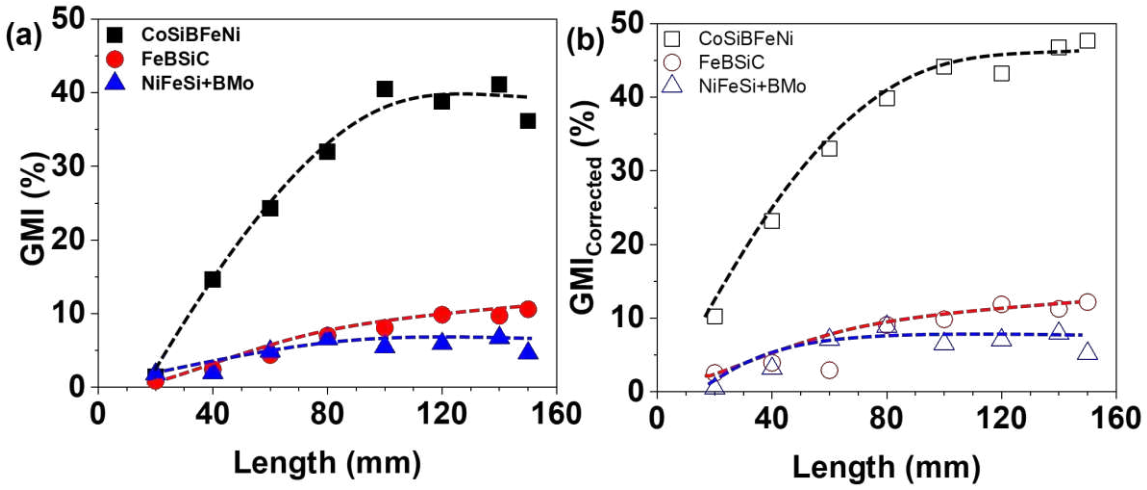

Fig. 6. (a) Variation of measured GMI ratio at f_0 with length for the Co-rich (black squares), Fe-rich (red circles) and Ni-rich (blue triangles) ribbons. (b) Equivalent data for $GMI_{corrected}$. All ribbons had width = 10 mm and thickness = 25 µm. Trendlines are plotted as guides to the eye.

The reduction of GMI ratio with decreasing ribbon length (and aspect ratio) was phenomenologically consistent with the results of previous studies on similar low aspect ratio ribbons [9], [11], [33], [36], where the effects of geometric variations are attributed to shape anisotropy. To support this conclusion, we calculated the in-plane demagnetization factors of the ribbon samples, N_x and N_y, as a function of ribbon length (Fig. 7). Here, the subscripts x and y represented directions along the length and width of the ribbon samples respectively. Fig. 7 also shows data for $(N_y – N_x)$, a factor proportional to the ribbons' in-plane shape anisotropy.

The data shown in Fig. 7 exhibited striking similarities to the form of the GMI data in Fig. 6. For example, both N_x and $(N_y – N_x)$ varied substantially for lengths below 80 mm, just as the GMI ratio did. Furthermore, at lengths over 80mm N_x, and $(N_y – N_x)$ both began to plateau. This was again consistent with measured GMI ratios which plateaued at a similar length [37]. Together these results provided strong evidence that the variation of GMI ratio with length was due to the effects of shape anisotropy, and that these effects were only significant in relatively low aspect ratio ribbons, i.e. those with aspect ratios less than 12 – 15. However, the physics underlying this was less clear. Shape anisotropy could have influenced the ribbons' transverse permeability in two distinct ways: Firstly, variations in the ribbons' demagnetising fields could have directly modified the transverse permeability of domain structures that remained essentially consistent as the ribbons' geometry changes

[38]. Secondly, changes in the ribbons' demagnetising fields may have modified the ribbons' domain structure, resulting in configurations that inherently exhibited lower transverse permeability [39]. Previous studies have favoured the latter explanation, suggesting that the variation of GMI with length was due to the formation of closure domains at the ends of the ribbons as their length decreased [9], [10], [23], [33]. These closure domains were theorised to reduce the transverse permeability of the ribbon, sharply reducing the GMI response. However, we do not believe that this hypothesis is definitively proven in the literature, and our own results do not offer us any further detailed insight into this question.

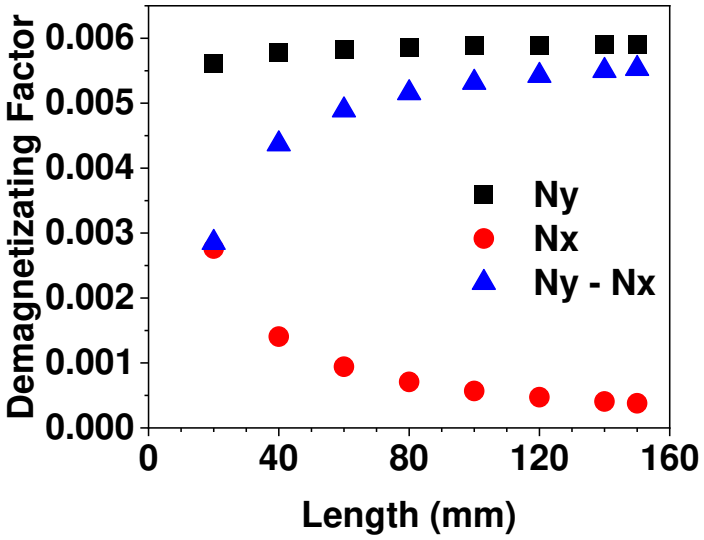

Fig. 7. Plots of N_y (black squares), N_x (red circles) and ($N_y - N_x$) (blue triangles) as a function of ribbon length. Calculations assume consistent ribbon widths = 10 mm and thicknesses = 25 µm.

b. Width dependence in high aspect ratio ribbons

Fig. 8 (a) presents the variation of the GMI ratio at f_0 with width for the Batch 4 (SLEC) ribbon samples. The Co-rich ribbons exhibited relatively little variation with a modest decrease in GMI ratio occurring at the largest widths. In contrast to this, the Fe-rich ribbon displayed a different behaviour with the GMI ratio increasing at small widths and becoming flatter at larger widths (around 8mm). The Ni-rich ribbons exhibited characteristics from both the Fe-rich and Co-rich ribbon trendlines: At low widths the GMI ratio increased until reaching a peak at approximately 6 mm, but at larger widths GMI ratios decreased with width. Fig. 8 (b) presents equivalent data for $GMI_{corrected}$. This

followed the same trends as the uncorrected dataset, suggesting parasitic impedances had very little effect on the observed results.

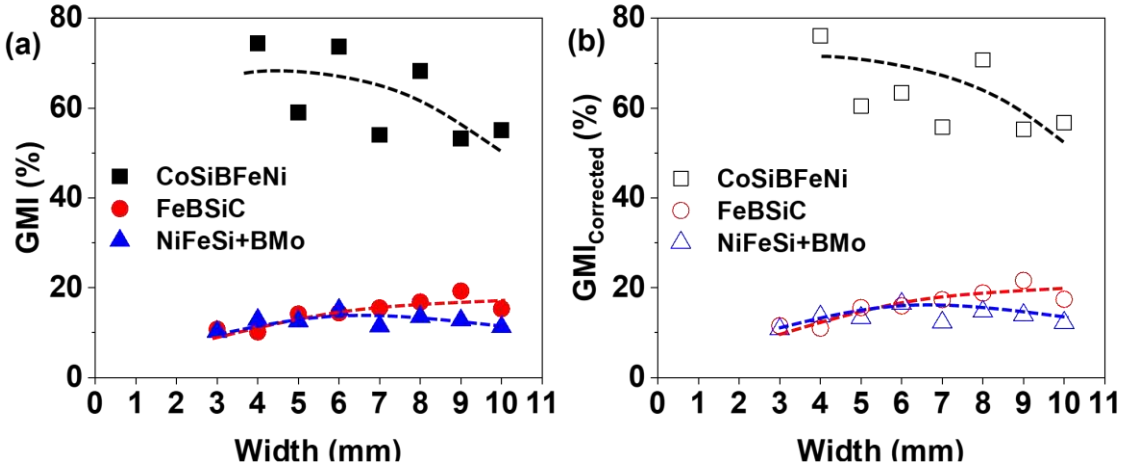

Fig. 8. (a) Variation of measured GMI ratio at f_0 with width for the Co-rich (black squares), Fe-rich (red circles) and Ni-rich (blue triangles) ribbons. (b) Equivalent data for $GMI_{corrected}$. All ribbons have length = 300mm and thickness = 25 µm. Trendlines are plotted as guides to the eye.

Following the example of our previous analysis we calculated the variation of N_x, N_y and (N_y – N_x) as a function of ribbon width (Fig. 9). These calculations showed that the transverse demagnetizing factor (N_y) increased rapidly as the ribbon width decreased, while N_x remained negligible. The overall effect of this was to produce a rapid growth in the ribbons' in-plane shape anisotropy (proportional to (N_y – N_x)) as their widths decreased. However, there appeared to be little correlation between the variations of the GMI ratio observed and the variation of demagnetising factors in these data series, indicating that shape anisotropy was not the primary origin of the trends seen in Fig. 8. We suggest that this was because, while the shape anisotropy was found to increase with decreasing ribbon width, it did so from an already high level, which was perhaps already sufficient to saturate any effects on the ribbons' magnetisation states and dynamics. Hence, it was believed that a different mechanism was contributing to the three distinct trends observed in the GMI ratio data.

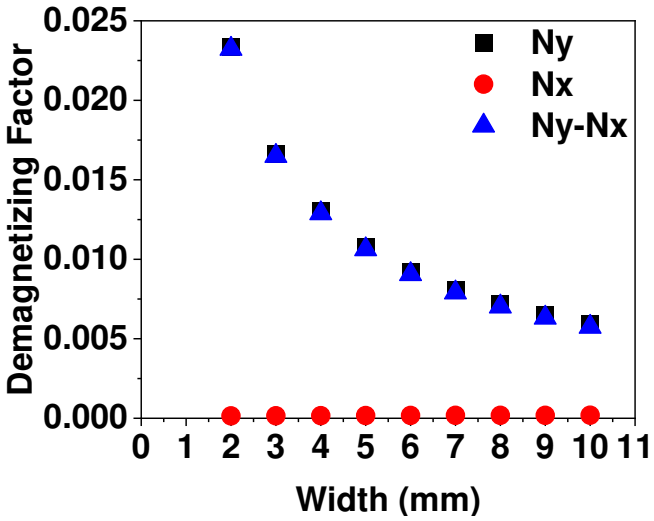

Fig. 9. Plots of N_y (black squares), N_x (red circles) and ($N_y - N_x$) (blue triangles) as a function of ribbon width. Calculations assume consistent ribbon length = 300mm and thicknesses = 25 µm.

To investigate whether the process of mechanically cutting the ribbons affected their GMI ratios we studied the width variation of GMI ratios in both SLEC and DLEC ribbons. Fig. 10(a – c) present the variation of f_0 and the GMI ratio at f_0 with width for both Batch 3 (DLEC) and 4 (SLEC) ribbon samples.

It was clear the different cutting processes had significant impacts on the samples' GMI ratios; the GMI ratios obtained for Batch 4 samples were consistently higher than those of Batch 3 samples. A possible explanation for this was that the primitive cutting process created strained regions at the edges of the ribbon. These would have induced local magnetoelastic anisotropies that may have either suppressed the transverse permeability directly, or indirectly through modification of the local domain structure. For example, the mixture of shear and tensile stress from the cutting motion may have induced a change in the orientation of the easy axis magnetisation within the ribbon samples. We can associate the cutting process with applying torsion to the edges of the ribbon samples. Livingston *et. al.* observed that, when they applied torsion to Fe-rich ribbon samples via twisting and untwisting, the orientation of the easy axis was different between the centre and at the edges of the ribbon samples [40]. Additionally, edge roughness created by the cutting process could also have contributed to a local reduction of the transverse permeability by pinning the magnetisation. A reduced transverse permeability at the edge of the ribbons would act to supress the contribution of these regions to the GMI effect, with the DLEC

ribbons having a greater proportion of their volume being affected, thus causing them to exhibit lower GMI ratios [41].

Despite the differences in the magnitudes of the GMI ratios between the Batch 3 (DLEC) and 4 (SLEC) ribbon samples, they showed very similar variations of their GMI ratios with width. Both the Fe-rich and Ni-rich ribbons exhibited sharp drops in their GMI ratio at low widths. We suggest that this trend was due to the damaged/strained edge regions accounting for progressively larger proportions of the ribbons' volume as their widths decreased. The differences in the trends observed for the three materials can be explained by their differing magnetostriction constants, λ_s: The Fe-rich ribbons had the highest λ_s and so showed the onset of a decreasing GMI ratio at the largest width (~8 mm). The Ni-rich ribbons had a lower (but still sizeable) λ_s and so the GMI ratios began to decrease at a lower width (~5 mm). The Co-rich ribbons had near zero λ_s and so did not show a decrease in GMI width within the studied range of geometries. We propose that the modest increases of GMI ratio with width observed at large widths in the Co-rich and Ni-rich ribbons are essentially a continuation of the trends due to shape anisotropy observed when measuring the samples in Batch 2. Indeed, as we will show below, all the batch 2 and 3 samples appear to form a continuous curve when plotted as a function of in-plane aspect ratio.

Another consistent feature observed in the Batch 3 and 4 samples was that f_0 decreased from ~2 MHz at small widths, to ~1 MHz at large widths. We are not sure of the underlying physics that caused this; however, it is likely to have been related to a shift in the balance of the mechanisms that contribute to the transverse susceptibility of the ribbons. For example, it is well established that domain wall motion becomes progressively damped as the frequency of excitation increase [2], [6], and so the observed trend may have been due to domain rotation becoming dominant in the lower width ribbons.

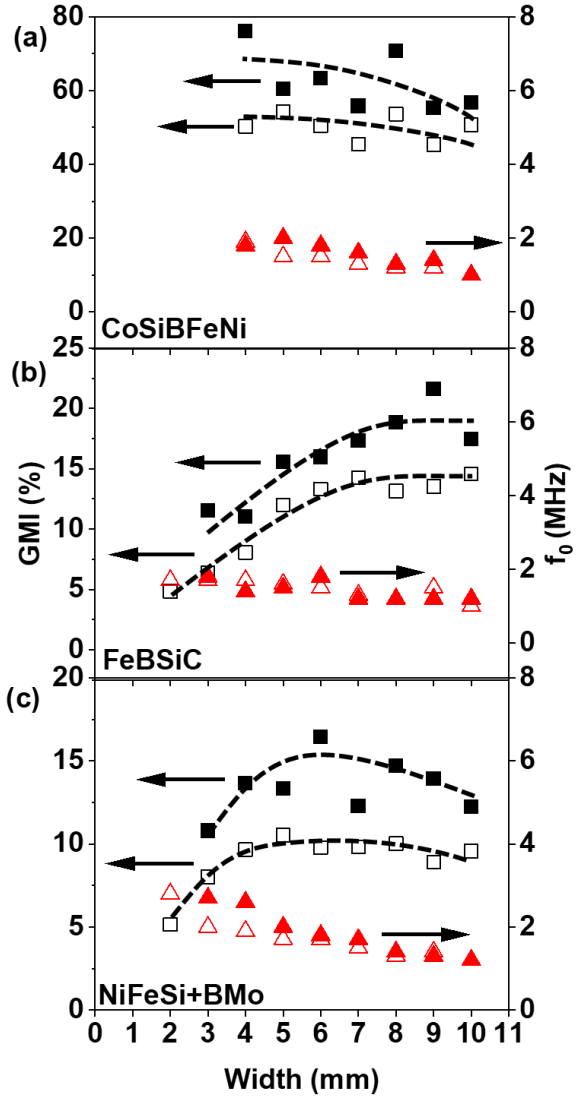

Fig. 10. Variation of GMI ratio (black squares) and critical frequency (f_0, red triangles) with ribbon width for ribbon samples composed of (a) $Co_{66}Si_{15}B_{14}Fe_4Ni_1$, (b) $Fe_{81}B_{13}Si_{3.5}C_2$ and (c) $Ni_{40}Fe_{40}Si+B_{19}Mo_{1\text{-}2}$. Data is shown for both Batch 3 (SLEC cut, closed symbols) and Batch 4 (DLEC cut, open symbols) ribbon samples. All ribbons have common lengths of 300 mm and thicknesses of 25 µm. Trendlines are shown as guides to the eye.

c. Variation of GMI ratio with aspect ratio

To unify the trends observed for the variation of GMI ratio with ribbon length and width we replotted the data as a function of the ribbons' aspect ratio (Fig. 11. (a)).

Data shown is for ribbon samples from Batches 3 and 4, as these had a consistent DLEC edge profile. Fig. 11. (b) presents equivalent data for $GMI_{corrected}$, which showed very similar trends to the uncorrected data.

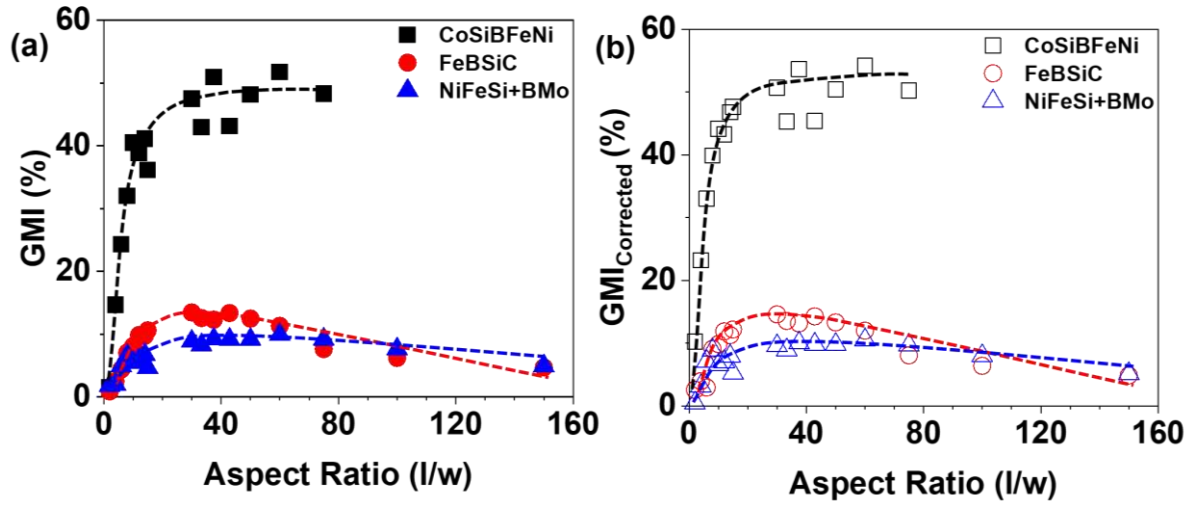

Fig. 11. (a) Peak GMI ratio as a function of in-plane aspect ratio (length/width). (b) Equivalent data for $GMI_{corrected}$.

For all three materials a continuous curve was observed. The Fe-rich and Ni-rich datasets ribbons exhibited a peaked form, as noted previously in section 3.2.b. We suggest that peak was the result of competition between the effects of strained/damaged edge regions and the global shape anisotropy. The increasing trend with aspect ratio for $l/w < 20$ was due to shape anisotropy. The decreasing trend with aspect ratio for l/w > 20 was caused by our primitive cutting method which suppressed the GMI ratio at lower widths (which translates to a high l/w). The Co-rich ribbons exhibited an asymptotic trend, which we attributed to its near-zero λ_s value.

3.3 Effects of heat treatment on SLEC and DLEC ribbons

To investigate whether the effects of our mechanical cutting process could be reversed by relaxing induced strains, we performed heat treatments of a SLEC ribbon and a DLEC Fe-rich ribbons with l = 180 mm, w = 4 mm and thickness = 25 µm. Fig. 11. (a) and (b) present the frequency-dependent GMI ratios for both, ribbon samples before and after heat treatment.

We observed that the differences between the GMI ratios of the SLEC and DLEC ribbon samples persisted even after annealing, with the SLEC ribbon maintaining notably higher GMI ratios than DLEC ribbon sample. Furthermore, there were differences in the degree to which the GMI ratio was enhanced by the heat treatment: the peak GMI ratio of the SLEC ribbon sample was enhanced by ~3.4%, while enhancement in the DLEC ribbon sample was ~1.4%. Many studies have correlated the effects of thermal treatment on a material's GMI ratio to the alleviation of internal stresses present in the sample from fabrication processes

[10], [22]. However, the heat treatment process applied here was clearly insufficient to completely restore parity between the GMI ratios of the SLEC and DLEC ribbons. Thus, we suggest that the differences in GMI behaviours between the SLEC and DLEC ribbon samples were caused either by inelastic deformations of the materials, or by edge roughness, induced by the crude mechanical cutting process used to prepare the ribbons.

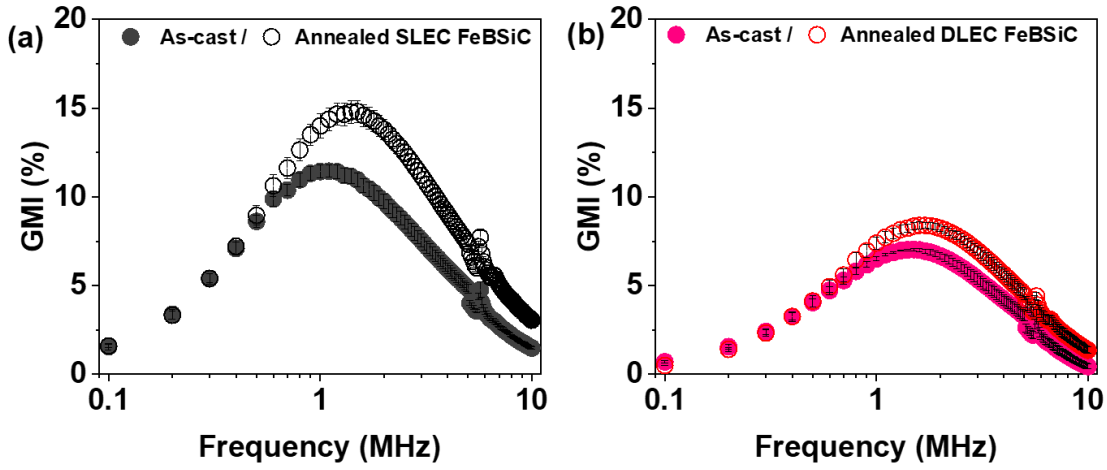

Fig. 12. GMI ratio vs frequency plots of as-cast and annealed (a) SLEC and (b) DLEC $Fe_{81}B_{13}Si_{3.5}C_2$ ribbons. The ribbons had length = 180 mm, width = 4 mm and thickness = 25μm.

4. Conclusion

In this paper we have studied the effects of geometry, cutting process and heat treatment on the GMI behaviour of ribbons composed of commercially available amorphous magnetic materials. We have studied the width and length dependence of the peak GMI ratio, as well as how the GMI response changes when either one (SLEC) or both sides (DLEC) of the ribbon were mechanical cut when preparing the ribbons from precursor foils.

Our results suggest that, as expected, the GMI ratio of the materials we studied was correlated to the size of their saturation magnetostriction coefficient λ_s, with low values promoting higher GMI ratios, even without additional field annealing. The roughness of the ribbon's surfaces may also have played a role in differentiating their GMI properties.

The geometry dependence of the GMI ratio was found to be complicated, with ribbons with non-zero λ_s constants exhibiting competition between the effects of shape anisotropy and those of edge regions damaged by a crude mechanical cutting process. In particular, we attributed a decrease in GMI ratios with width in high aspect ratio ribbons to magneto-

elastic anisotropies or roughness induced at the edges of the ribbons during the cutting process. This conclusion is reinforced by comparison between the GMI behaviour of SLEC and DLEC ribbons, where it was found that SLEC ribbons always exhibited higher GMI ratios. Experiments in which the ribbons were heat treated after cutting enhanced the ribbons' GMI ratios, most likely due to the relaxation of induced strains, but were unable to restore parity between the SLEC and DLEC cut ribbons. GMI was found to increase with increasing length for aspect ratios *l/w* less than ~20, which we attributed to the effects of shape anisotropy. In combination, these two effects produce trends that were consistent with other works where a 'critical aspect ratio' that maximised the GMI ratio was observed [9], [10], although we have proposed alternative explanations for these phenomena in our samples.

Most significantly for applications, our results suggest that high GMI ratios can be maintained in high aspect ratio ribbons even when prepared from commercially available materials using relatively primitive cutting processes. This suggest such ribbons could be successfully deployed as macro-scale sensors where either small magnetic fields/strain must be detected over large sensing areas, or where more acute local stimuli must be detected if they occur at any point in a larger region of sensor coverage.

Acknowledgements

The authors thank the Nuclear Decommissioning Authority (NDA) for funding this project and the Henry Royce Institute for Advanced Materials, funded through EPSRC grants EP/R00661X/1, EP/S019367/1, EP/P02470X/1 and EP/P025285/1, for the financial support and Bruker Fastscan AFM access at The University of Sheffield.

Data Availability

The data that supports the findings of this study are available within the article.

References

[1] C. Morón, C. Cabrera, A. Morón, A. Garcí, and M. González, "Magnetic Sensors Based on Amorphous Ferromagnetic Materials: A Review," *Sensors*, vol. 15, pp. 28340–28366, 2015.

[2] M. H. Phan and H. X. Peng, "Giant magnetoimpedance materials: Fundamentals and applications," *Progress in Materials Science*. 2008.

[3] M. Knobel and K. R. Pirota, "Giant magnetoimpedance: Concepts and recent progress," *Journal of Magnetism and Magnetic Materials*. 2002.

[4] S. Dwevedi, G. Markandeyulu, P. R. Ohodnicki, A. Leary, and M. E. McHenry, "Stress-

MI and domain studies in Co-based nanocrystalline ribbons," *J. Magn. Magn. Mater.*, vol. 323, no. 15, pp. 1929–1933, Aug. 2011.

[5] J. Hu, H. Qin, J. Chen, and Y. Zhang, "Giant stress-impedance effect in Fe73.5CuNb3-xV xSi13.5B9 amorphous ribbons," *J. Magn. Magn. Mater.*, 2003.

[6] M. Knobel, M. Vázquez, and L. Kraus, "Giant Magnetoimpedance," *Handb. Magn. Mater.*, vol. 15, pp. 497–563, Jan. 2003.

[7] V. Zhukova *et al.*, "Effect of Nanocrystallization on Magnetic Properties and GMI Effect of Fe-rich Microwires," *J. Electron. Mater.*, 2014.

[8] H. Q. Guo, H. Kronmüller, T. Dragon, Z. H. Cheng, and B. G. Shen, "Influence of nanocrystallization on the evolution of domain patterns and the magnetoimpedance effect in amorphous Fe73.5Cu1Nb3Si13.5B9 ribbons," *J. Appl. Phys.*, vol. 89, 2001.

[9] A. Chaturvedi, T. P. Dhakal, S. Witanachchi, A. T. Le, M. H. Phan, and H. Srikanth, "Critical length and giant magnetoimpedance in Co69Fe 4.5Ni1.5Si10B15 amorphous ribbons," *Mater. Sci. Eng. B Solid-State Mater. Adv. Technol.*, 2010.

[10] Y. H. Ding, K. Xue, W. Y. Wang, and X. Ma, "Influence of aspect ratio on giant magnetoimpedance effect for Fe67Co18Si11B4 amorphous ribbons," *Acta Metall. Sin. (English Lett.*, vol. 30, no. 12, pp. 1236–1242, 2017.

[11] K. C. Mendes, "Enhanced GMI in ribbons of Co70.4Fe4.6Si1.5B10 alloy," vol. 181, pp. 111–112, 1998.

[12] M. Zhao, S. Fang, Z. Han, J. Wei, H. Peng, and L. Chen, "Sample Length Dependence of Giant Magnetoimpedance in FeCuNbSiB Nanocrystalline Ribbons," vol. 48, no. 3, pp. 460–464, 2007.

[13] C. Zhao, X. Zhang, Q. Liu, and J. Wang, "GMI field sensitivity near a zero external field in Co-based amorphous alloy ribbons : experiments and model," 2016.

[14] L. González-Legarreta *et al.*, "Magnetoimpedance dependence on width in Co66.5Fe 3.5Si12.0B18.0 amorphous alloy ribbons," *J. Appl. Phys.*, vol. 113, no. 5, pp. 0–6, 2013.

[15] L. A. P. Gonc, J. M. Soares, F. L. A. Machado, and W. M. De Azevedo, "GMI effect in the low magnetostrictive Co 70 Fe 5 Si 15 B 10 alloys," vol. 384, pp. 152–154, 2006.

[16] K. R. Pirota, M. L. Sartorelli, M. Knobel, J. Gutierrez, and J. M. Barandiarah, "Influence of induced anisotropy and magnetostriction on the giant magnetoimpedance e!ect and its aftere!ect in soft magnetic amorphous ribbons," *J. Magn. Magn. Mater.*, vol. 202, pp. 431–444, 1999.

[17] H. Chiriac and T. A. Óvári, "Amorphous glass-covered magnetic wires: Preparation, properties, applications," *Prog. Mater. Sci.*, vol. 40, no. 5, pp. 333–407, Jan. 1996.

[18] A. Zhukov *et al.*, "Manipulation of magnetic properties of glass-coated microwires by annealing," *J. Magn. Magn. Mater.*, 2015.

[19] A. Zhukov *et al.*, "Effect of annealing on magnetic properties and magnetostriction coefficient of Fe-Ni-based amorphous microwires," *J. Alloys Compd.*, 2015.

[20] M. H. Phan, H. X. Peng, M. R. Wisnom, S. C. Yu, C. G. Kim, and N. H. Nghi, “Effect of annealing temperature on permeability and giant magneto-impedance of Fe-based amorphous ribbon,” *Sensors Actuators A*, vol. 129, pp. 62–65, 2006.

[21] A. Chaturvedi, T. P. Dhakal, S. Witanachchi, A. T. Le, M. H. Phan, and H. Srikanth, “Critical length and giant magnetoimpedance in Co69Fe 4.5Ni1.5Si10B15 amorphous ribbons,” *Mater. Sci. Eng. B Solid-State Mater. Adv. Technol.*, vol. 172, no. 2, pp. 146–150, 2010.

[22] F. Jin, L. Zhou, W. Cheng, Y. Zhang, B. Tong, and Y. Xu, “Effect of Shape and Annealing on the Giant Magnetoimpendence Properties of FeCoSiB Ribbon,” *IEEE Trans. Magn.*, vol. 50, no. 10, pp. 1–4, 2014.

[23] Y. Ding, R. Tian, K. Xue, X. Wang, Y. Shi, and X. Ma, “Impact of ribbon width on magnetoimpedance and permeability of Fe69.2Co7.7Cu0.6Nb2.5Si11B9 soft magnetic alloy,” *Mater. Technol.*, vol. 31, no. 6, pp. 337–341, 2016.

[24] “Cobalt/Silicon/Boron/Iron/Nickel Foil CO810250 - Goodfellow Catalog.” [Online]. Available: http://www.goodfellow.com/catalogue/GFCat4I.php?ewd_token=t5Hi55VEn7gmigQ8omoaE3EsYo1a6W&n=H8vrxrqtUtiolf3A3HDcEcWGNXdgOH&ewd_urlNo=GFCat4B11&Catite=CO810250&CatSearNum=5. [Accessed: 09-Oct-2019].

[25] “Iron/Boron/Silicon Foil FE800250 - Goodfellow Catalog.” [Online]. Available: http://www.goodfellow.com/catalogue/GFCat4I.php?ewd_token=t5Hi55VEn7gmigQ8omoaE3EsYo1a6W&n=H8vrxrqtUtiolf3A3HDcEcWGNXdgOH&ewd_urlNo=GFCat4B11&Catite=FE800250&CatSearNum=5. [Accessed: 09-Oct-2019].

[26] “Nickel/Boron/Silicon Foil NI800250 - Goodfellow Catalog.” [Online]. Available: http://www.goodfellow.com/catalogue/GFCat4I.php?ewd_token=t5Hi55VEn7gmigQ8omoaE3EsYo1a6W&n=H8vrxrqtUtiolf3A3HDcEcWGNXdgOH&ewd_urlNo=GFCat4B11&Catite=NI800250&CatSearNum=5. [Accessed: 09-Oct-2019].

[27] L. Jin, S. S. Yoon, P. Kollu, C. G. Kim, D. S. Suhr, and C. O. Kim, “Dependence of GMI Profile on Size of Co-based Amorphous Ribbon,” *J. Magn.*, vol. 12, no. 1, pp. 31–34, 2007.

[28] V. Raposo, J. I. Iñiguez, D. García, A. G. Flores, and M. Vázquez, “Internal magnetoimpedance of amorphous wires,” in *Intermag 2003 - Program of the 2003 IEEE International Magnetics Conference*, 2003.

[29] P. Gazda and R. Szewczyk, “Novel Giant Magnetoimpedance Magnetic Field Sensor,” *Sensors*, vol. 20, no. 3, pp. 1–15, 2020.

[30] C. Zhao, X. Zhang, Q. Liu, and J. Wang, “GMI field sensitivity near a zero external field in Co-based amorphous alloy ribbons: Experiments and model,” *J. Phys. D. Appl. Phys.*, vol. 49, no. 6, 2016.

[31] D. García, V. Raposo, O. Montero, and J. I. Íñiguez, “Influence of magnetostriction constant on magnetoimpedance–frequency dependence,” *Sensors Actuators A Phys.*, vol. 129, no. 1–2, pp. 227–230, May 2006.

[32] M. Knobel, M. L. Sanchez, J. Velazquez, and M. Vazquez, “Stress dependence of the

giant magneto-impedance effect in armorphous wires," p. 7, 1995.

[33] M. Zhao, S. Fang, Z. Han, J. Wei, H. Peng, and L. Chen, "Sample length dependence of giant magnetoimpedance in FeCuNbSiB nanocrystalline ribbons," *Mater. Trans.*, vol. 48, no. 3, pp. 460–464, 2007.

[34] A. Chaturvedi, T. Dhakal, S. Witanachchi, A. T. Le, M. H. Phan, and H. Srikanth, "Correlation between magnetic softness, sample surface and magnetoimpedance in Co69Fe4.5X1.5Si10B15(X=Ni, Al, Cr) amorphous ribbons," *Phys. B Condens. Matter*, 2010.

[35] T. Eggers *et al.*, "Impact of the transverse magnetocrystalline anisotropy of a Co coating layer on the magnetoimpedance response of FeNi-rich nanocrystalline ribbon," *J. Alloys Compd.*, vol. 741, pp. 1105–1111, 2018.

[36] Z. M. Wu *et al.*, "Magnetoelastic resonance enhancement of longitudinally driven giant magnetoimpedance effect in FeCuNbSiB ribbons," *Phys. B Condens. Matter*, 2010.

[37] A. Aharoni, "Demagnetizing factors for rectangular ferromagnetic prisms," *J. Appl. Phys.*, vol. 83, no. October 1997, pp. 3432–3434, 1998.

[38] C. Zhao, L. Pan, X. Li, L. Ma, Q. Liu, and J. Wang, "Optimization of magnetoimpedance effect in Co-based ribbon by laser patterning for sensor arrays application," *J. Phys. D. Appl. Phys.*, vol. 51, no. 4, 2018.

[39] T. Eggers *et al.*, "Correlation between domain structure, surface anisotropy and high frequency magneto-impedance in Joule annealed CoFe-based melt-spun ribbons," *J. Alloys Compd.*, 2016.

[40] J. D. Livingston and W. G. Morris, "Magnetic domains in twisted amorphous ribbons," *IEEE Trans. Magn.*, vol. 20, no. 5, pp. 1379–1381, 1984.

[41] H. T. Tran *et al.*, "Anisotropic Mechanical and Giant Magneto-Impedance Properties of Cobalt-Rich Amorphous Ribbons," vol. 45.